

Structural, Electrical and Electrochemical Characterizations of Perovskite Ni-Doped $\text{SrCoO}_{3-\delta}$

Sofiane Makhoulfi¹ · Mahmoud Omari¹

Received: 19 June 2015 / Accepted: 9 October 2015 / Published online: 13 October 2015
© Springer Science+Business Media New York 2015

Abstract Perovskite $\text{SrCo}_{1-y}\text{Ni}_y\text{O}_{3-\delta}$ ($0 \leq y \leq 0.4$) oxides synthesized by sol–gel method were investigated. X-ray diffraction, thermogravimetric and differential thermal analysis, fourier transform infrared spectroscopy, scanning electron microscopy, electrical conductivity and electrochemical measurements, were used to characterize the structure, morphology, electrical and electrochemical properties of the samples. The studied compounds have rhombohedral crystal structure in the substitution range $0 \leq y \leq 0.4$ and the solubility of Ni in the $\text{SrCoO}_{3-\delta}$ was limited to $y \leq 0.3$. Temperature dependence of electrical conductivity shows a semiconducting behavior. The conductivity increases with increasing nickel substitution and reaches a maximum for the composition of $\text{SrCo}_{0.7}\text{Ni}_{0.3}\text{O}_{3-\delta}$ (19 S cm^{-1}) at $300 \text{ }^\circ\text{C}$. The electrochemical measurements indicate that the catalytic activity is strongly influenced by nickel doping. The highest electrode performance is achieved with large nickel content.

Keywords Perovskite oxide · Sol–gel · Powder diffraction · Thermal analysis · Electrical conductivity · Electrochemical properties

1 Introduction

Perovskite-type oxides have attracted great interest in both applied and fundamental areas of solid state chemistry, physics, advanced materials, and catalysis [1]. The family

of compounds with ABO_3 structure containing strontium and cobalt in their A and B sites, respectively has received a great attention due to their high electronic conductivity and oxygen ionic conductivity [2–4].

$\text{SrCoO}_{3-\delta}$ composite is an important parent compound for the development of a series of functional materials. Depending on the operating temperature, oxygen partial pressure of the environment, thermal history, and synthesis method, strontium cobaltite present 2-H type hexagonal perovskite, oxygen vacancy-ordered brownmillerite, rhombohedral perovskite, or cubic perovskite structure [5–7]. Another study has revealed that the phase structure and electrical conductivity of $\text{SrCoO}_{3-\delta}$ oxide were closely related with the oxygen content in the composite [8].

These complex oxides can be properly modified by the partial substitution of atoms at A and/or B sites which may affect strongly their physical properties. Indeed, depending on the doping component and level, the material can display ferromagnetic or thermo-electrical properties [9] and electrochemical properties [2, 4]. $\text{SrCoO}_{3-\delta}$ doped with various metal ions such as Nb [10], Sc [11], Sb [4], Ca and Fe [7], Ce and Fe [2, 12], were previously studied. These oxides have been identified as promising IT-SOFC cathode materials and oxygen transport membranes.

A few years ago, several studies have shown that nickel catalysts were active for reforming of methane [13–15]. On the other hand, another work on Ni-doped perovskite anodes for oxidation of hydrogen in IT-SOFC has been carried out [16]. It has been revealed that suitable power densities of about 420 mW cm^{-2} for the direct oxidation of hydrogen were achieved at $800 \text{ }^\circ\text{C}$.

Despite these advantages, there have been no reports to date concerning the synthesis and characterization of nickel doped strontium cobaltite oxides. In the present work, we examine the effect of partial substitution of cobalt by

✉ Mahmoud Omari
m.omari@univ-biskra.dz

¹ Laboratory of Molecular Chemistry and Environment,
University of Biskra, BP 145, 07000 Biskra, Algeria

nickel on structural, grain morphology, electrical conductivity and electrochemical properties of $\text{SrCo}_{1-y}\text{Ni}_y\text{O}_{3-\delta}$ ($0 \leq y \leq 0.4$) oxides prepared by the sol–gel method.

2 Experimental Procedure

2.1 Synthesis of Perovskite-Type Oxides

Ni-doped $\text{SrCoO}_{3-\delta}$ oxides were prepared by a sol–gel process. Highly pure (>99 % purity) $\text{Ni}(\text{NO}_3)_2 \cdot 6\text{H}_2\text{O}$ (BIOCHEM), $\text{Sr}(\text{NO}_3)_2$ (BIOCHEM), $\text{Co}(\text{NO}_3)_2 \cdot 6\text{H}_2\text{O}$ (BIOCHEM), and citric acid (JANSSEN CHIMICA) were used as raw materials. Stoichiometric amounts of $\text{Sr}(\text{NO}_3)_2$, $\text{Ni}(\text{NO}_3)_2 \cdot 6\text{H}_2\text{O}$ and $\text{Co}(\text{NO}_3)_2 \cdot 6\text{H}_2\text{O}$ based on the composition of $\text{SrCo}_{1-y}\text{Ni}_y\text{O}_{3-\delta}$ ($0 \leq y \leq 0.4$) were dissolved in a citric acid aqueous. The solution with metal ions and citric acid in the molar ratio of 1:1.2 was slowly stirred, heated at 80 °C for 5 h, and subsequently evaporated at 110 °C for 12 h. The resulting precursor is then milled and calcined in air for 6 h at different calcination temperatures: 650, 750, 850 and 950 °C with a heating rate of 5 °C min^{-1} .

2.2 Characterization Techniques

The thermal decomposition processes of the precursor gels were studied in air atmosphere by thermogravimetric and differential thermal analyses thermogravimetric and differential thermal analysis (TG/DTA) using a LINSEIS STA PT1600 at a heating rate of 10 °C min^{-1} in air. The Fourier transform infrared (FT-IR) absorption spectra were recorded using FT-IR SHIMADZU 8400S spectrometer. X-ray diffraction (XRD) characterization of samples was carried out with a D8 Advance Bruker using a Cu K_α line at 0.1540 nm in the range of 20°–70° in steps of 0.025 at a scan speed 2° min^{-1} . Moreover, morphological aspects of the powders were examined by using a ESEM-FEI Quanta 600 FEG scanning electron microscope.

The electrical conductivity was measured using the standard d.c. four-probe method. The sample was heated using a cryostat (Janis Inc.). The voltage was measured using a sensitive (V–I) source (Keithley 2182) with accuracy better than 10 μV . In all measurements, the temperature was raised slowly to the required temperature at which the V–I characteristics were measured.

The electrochemical experiments for O_2 reduction and evolution were performed using a Volta Lab 40 potentiostat/galvanostat. The measurements were carried out in a three-compartment cell. Potassium hydroxide electrolyte solution (1 M) was prepared by dissolving the required amount of KOH (Merck) into bidistilled water. The working electrodes (1 cm^2) were obtained by painting,

with an oxide suspension. The loading of catalyst films was $12 \pm 3 \text{ mg cm}^{-2}$ in each case. The counter electrode used was a Pt plate. The reference electrode was Hg/HgO/1 M KOH. All potentials in the text have been referred to this reference electrode.

3 Results and Discussions

3.1 Thermal Analysis

The mechanism of the thermal decomposition in flowing air of $\text{SrCo}_{0.9}\text{Ni}_{0.1}\text{O}_{3-\delta}$ precursor gel was studied by TG/DTA measurements. The TG/DTA profiles for this sample are shown in Fig. 1. In TG curve, there are four regions of weight loss: (1) 25–100 °C, (2) 100–200 °C, (3) 200–540 °C, and (4) 820–920 °C with corresponding organic weight losses of 5, 8, 40 and 8 %, respectively. At the first region of weight loss, water and gases adsorbed on the powder surface were eliminated, with an endothermic transition at 80 °C. The second region of mass loss, can be ascribed to the removal of the residual water and a partial decomposition of citric acid chain [17], accompanied a broad exothermic peak around 180 °C in DTA curve. The third step was assigned to the combustion of the organic material between 200 and 540 °C (mass loss –40 %), with a strong and large exothermic peak in the DTA curve, which contains two endothermic peaks. These peaks probably correspond to the formation of the strontium carbonate [18]. The last small endothermic peak was observed at about 870 °C, can be attributed to the formation of the $\text{SrCo}_{0.9}\text{Ni}_{0.1}\text{O}_{3-\delta}$ crystal, as was confirmed by XRD results, discussed below.

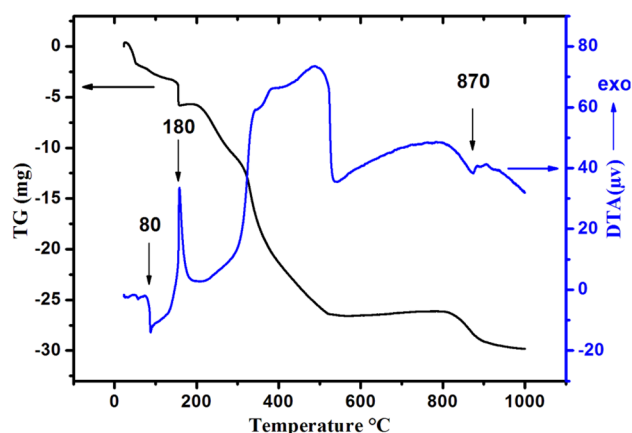


Fig. 1 TG and DTA curves of $\text{SrCo}_{0.9}\text{Ni}_{0.1}\text{O}_{3-\delta}$ precursor heated in air at 10 °C min^{-1}

3.2 X-ray Diffraction

XRD experiments were first performed to check the phase purity of the materials. Figure 2 shows the XRD patterns of the $\text{SrCo}_{1-y}\text{Ni}_y\text{O}_{3-\delta}$ (SCNy, $y = 0, 0.1, 0.2, 0.3$ and 0.4), sintered at 950°C for 6 h in air. The samples with $y \leq 0.3$ were found to be single phase and all the reflections were indexed on the basis of rhombohedral perovskite structure (PDF card 00-049-0692), with no detectable secondary phase. For $y = 0.4$, the main phase was also rhombohedral perovskite with another minor phase $\text{Sr}_5\text{Ni}_4\text{O}_{11}$ (PDF card 00-042-0521) was formed, indicating a Ni solubility limit of ~ 0.3 in the $\text{SrCo}_{1-y}\text{Ni}_y\text{O}_{3-\delta}$ system.

The authors [19, 20] suggest a hexagonal BaNiO_3 -type structure, but they could not index all the diffraction maxima on their XRD pattern. At the same time, Rodriguez et al. [21, 22] have shown a possibility to describe the same set of d-spacings as a rhombohedral cell and have provided evidence for good agreement of all the observed and calculated values. In this study, the structure of the low-temperature form of strontium cobaltite will be referred to the rhombohedral (R) (PDF card 00-049-0692).

Figure 3 shows the magnified part of the diffraction peaks of Ni-doped $\text{SrCoO}_{3-\delta}$. These peaks with 2θ around 32.6° can be indexed to the (300) reflection of the rhombohedral perovskite structure. As can be seen, the peaks were shifted to the high angles with increasing Ni concentration for the doped samples.

The lattice parameters of the perovskites $\text{SrCo}_{1-y}\text{Ni}_y\text{O}_{3-\delta}$ were calculated for each y value from the XRD patterns using Celref programme. The phase compositions, lattice parameters and unit cell volumes of the investigated samples after heat treatment at 950°C are summarized in

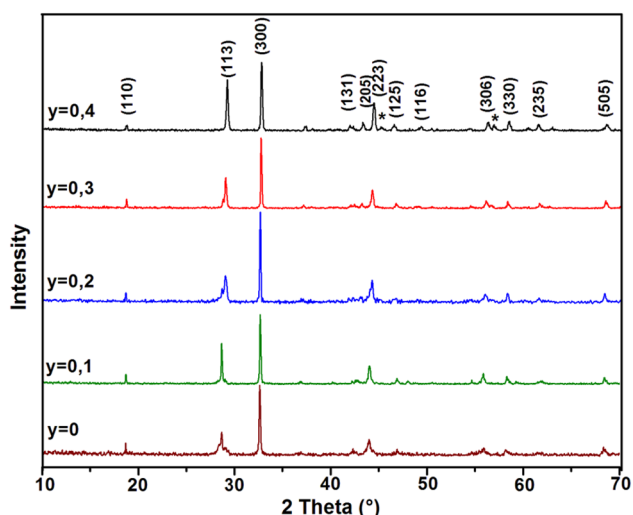


Fig. 2 XRD patterns of the $\text{SrCo}_{1-y}\text{Ni}_y\text{O}_{3-\delta}$ ($0.0 \leq y \leq 0.4$) samples calcined at 950°C . **R** rhombohedral phase; * $\text{Sr}_5\text{Ni}_4\text{O}_{11}$

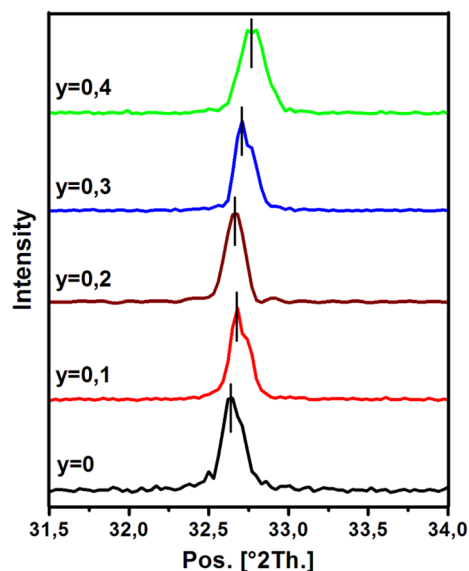


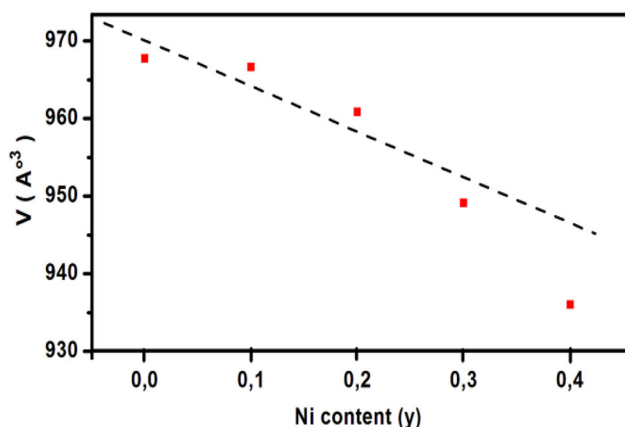
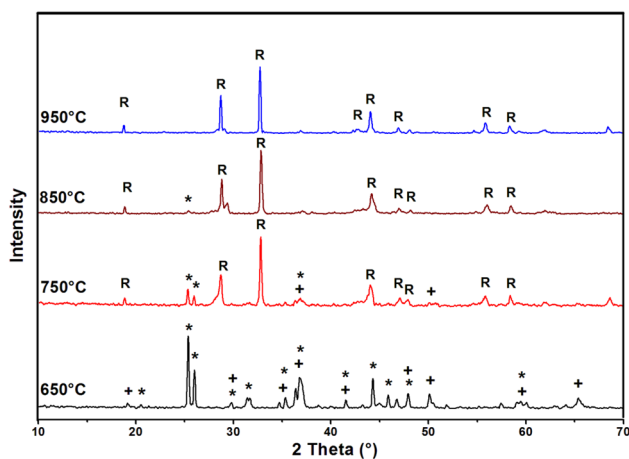
Fig. 3 Evolution of the position of the highest X-ray diffraction peak

Table 1. The lattice parameters of the perovskite decrease slightly with increasing y from 0 to 0.4. This is due to the substitution of the larger Co ions by the smaller Ni ions, since the ionic radius of the Co^{+2} and Ni^{+2} in six-coordination are 0.072 and 0.069 nm, respectively [23]. Similar tendency has been found previously for $\text{La}_{0.9}\text{Sr}_{0.1}\text{Ga}_{1-x}\text{Ni}_x\text{O}_{3-\delta}$ samples [24]. The unit cell volume as a function of Ni content after treating the samples in air is shown in Fig. 4. A linear relationship between unit cell volume and the Ni content is observed for $y \leq 0.3$, in agreement to Vegard's law for solid solutions. Conversely, the composition with $y = 0.4$ does not follow this trend because this is not a pure phase.

Figure 5 shows the XRD patterns of $\text{SrCo}_{0.9}\text{Ni}_{0.1}\text{O}_{3-\delta}$ calcined at different temperatures for 6 h. After calcination at 650°C , the precursor is a mixture containing orthorhombic SrCO_3 (PDF: 01-074-1491) and spinel Co_3O_4 (PDF: 01-076-1802). When the precursor was heated at 750°C in air for 6 h, the characteristic diffraction peaks of Co_3O_4 and SrCO_3 become weaker while those of rhombohedral structure appear. With the increase of calcination temperature, the intensity of characteristic diffraction peaks of Co_3O_4 and SrCO_3 becomes weaker at 850°C and disappears at 950°C . The intensity of characteristic diffraction peaks of rhombohedral structure becomes stronger and no reflections from strontium oxide and nickel oxide are observed as distinct intermediate phases to the formation of $\text{SrCo}_{0.9}\text{Ni}_{0.1}\text{O}_{3-\delta}$ during the thermal decomposition of the precursor powder. After heat treatment at 950°C , the precursor shows good crystallinity of the rhombohedral structure of $\text{SrCo}_{0.9}\text{Ni}_{0.1}\text{O}_{3-\delta}$. These XRD patterns confirm that all samples maintain the

Table 1 Values of unit cell parameters for pure and substituted $\text{SrCoO}_{3-\delta}$

Nominal compositions	a = b (Å)	c (Å)	V (Å ³)
$\text{SrCoO}_{3-\delta}$	9.5051 ± 0.0003	12.3682 ± 0.0006	967.73 ± 0.03
$\text{SrCo}_{0.9}\text{Ni}_{0.1}\text{O}_{3-\delta}$	9.4936 ± 0.0001	12.3842 ± 0.0003	966.63 ± 0.01
$\text{SrCo}_{0.8}\text{Ni}_{0.2}\text{O}_{3-\delta}$	9.4796 ± 0.0003	12.3460 ± 0.0004	960.81 ± 0.03
$\text{SrCo}_{0.7}\text{Ni}_{0.3}\text{O}_{3-\delta}$	9.4903 ± 0.0002	12.1684 ± 0.0006	949.13 ± 0.02
$\text{SrCo}_{0.6}\text{Ni}_{0.4}\text{O}_{3-\delta}$	9.4782 ± 0.0003	12.0310 ± 0.0005	936.03 ± 0.03

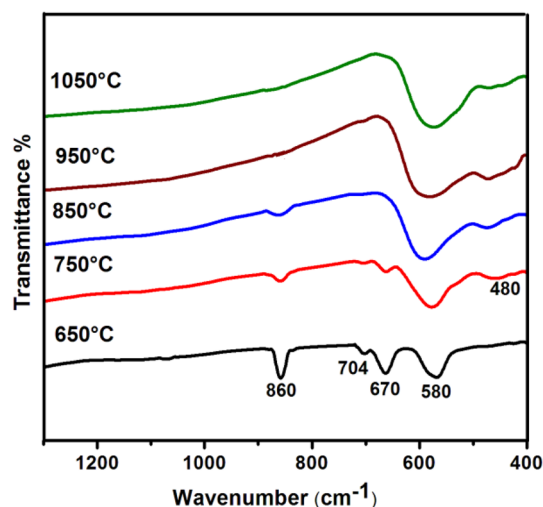
**Fig. 4** Variation of the unit cell volume for $\text{SrCo}_{1-y}\text{Ni}_y\text{O}_{3-\delta}$ as a function of the Ni content**Fig. 5** XRD patterns of the $\text{SrCo}_{0.9}\text{Ni}_{0.1}\text{O}_{3-\delta}$ at different temperatures. (R): rhombohedral phase; (+): Co_3O_4 ; (*): SrCO_3

rhombohedral perovskite structure (PDF card 00-049-0692) at temperatures higher than 650 °C.

3.3 IR Spectroscopy

The vibration frequencies in the infrared region are fundamental for the control of the reaction process and properties of materials. Fourier transformed infrared spectroscopy results of $\text{SrCo}_{0.9}\text{Ni}_{0.1}\text{O}_{3-\delta}$ precursor

calcined at different temperatures are shown in Fig. 6. Five bands were observed at 860, 704, 670, 580 and 480 cm^{-1} . At 650 °C, the IR spectra show two strong absorption bands at 670 and 580 cm^{-1} , which confirms the formation of the spinel structure of Co_3O_4 [25–27]. The first peak is attributed to the stretching vibration mode of M–O in which M is Co^{2+} and is tetrahedrally coordinated [28–30]. The second peak can be assigned to M–O in which M is Co^{3+} and is octahedrally coordinated [28–30]. The bands at 860 cm^{-1} , 704 cm^{-1} corresponding to the respective ν_2 and ν_4 modes of carbonate [31], mark the existence of SrCO_3 [32]. At temperatures higher than 750 °C, the content of SrCO_3 decreases and another band at 480 cm^{-1} appears which is characteristic of the rhombohedral perovskite structure. This result further confirms that SrCO_3 keep on joining into Co_3O_4 structure and form the perovskite oxide. A similar result was found in $\text{Ba}(\text{Fe},\text{Co})\text{O}_{3-\delta}$ [33]. It has been shown that BaCO_3 will keep on joining into CoO_6 and form the compound $\text{BaCoO}_{2.93}$. These results are in accordance with the XRD analysis (Fig. 5). The bands at 860, 704, and 670 cm^{-1} disappear when the precursor was calcined at 950 °C in air which indicates that the decomposition of carbonate has finished. The bands at 580 and 480 cm^{-1} due to the asymmetric stretching vibrations of Sr–O and Co–O groups [34–36].

**Fig. 6** Infrared spectra of $\text{SrCo}_{0.9}\text{Ni}_{0.1}\text{O}_{3-\delta}$ calcined at different temperatures

This is in accordance with the XRD results (Fig. 5) which confirms the formation of a single crystalline phase in $\text{SrCo}_{0.9}\text{Ni}_{0.1}\text{O}_{3-\delta}$ nanopowder.

Figure 7 shows the IR spectra of $\text{SrCo}_{1-y}\text{Ni}_y\text{O}_{3-\delta}$ ($y = 0, 0.1, 0.2, 0.3$ and 0.4) gels heated at 950°C for 6 h. Two strong absorption bands were observed around 580 and 480 cm^{-1} . The higher frequency band was assigned to the M–O stretching vibration mode (possible Sr–O, Co–O or Ni–O stretching frequencies vibrations) [34, 35] and the lower one corresponds to the bending mode which is sensitive to a change in the M–O–M bond angle (M=Co or Ni). Similar results have been found previously for $\text{La}_{1-x}\text{Ca}_x\text{CoO}_3$ [37], $\text{LaCo}_x\text{Fe}_{1-x}\text{O}_3$ and $\text{LaNi}_x\text{Fe}_{1-x}\text{O}_3$ oxides [38]. These two bands are related to the environment surrounding the MO_6 octahedral in the ABO_3 perovskite [39]. The IR spectra of samples calcined at 950 and 1050°C do not show any band attributable to carbonates and only M–O and M–O–M stretching frequencies are observed. These results are consistent with the crystallization process observed by TG/DTA and XRD measurements.

3.4 Structural and Morphological Characterization

The peak broadening at lower angle is more meaningful for the calculation of particle size, therefore size of nanocrystals. The crystallite size (D_{hkl}) of the samples was calculated from the full width at half maximum of the most intense diffraction peak using Scherrer's equation (Eq. 1) [40]:

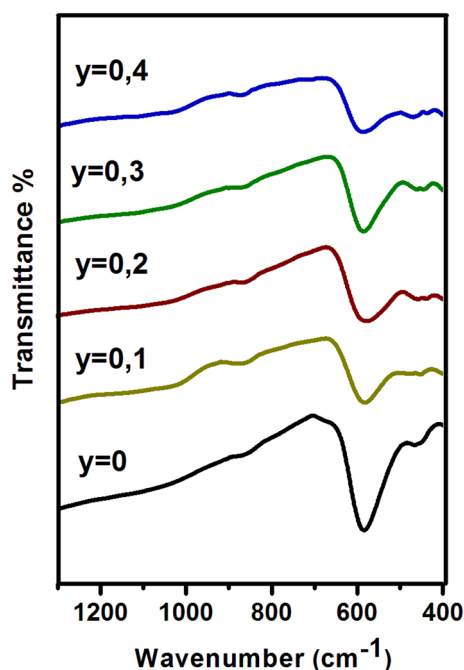


Fig. 7 Infrared spectra of $\text{SrCo}_{1-y}\text{Ni}_y\text{O}_{3-\delta}$ ($0.0 \leq y \leq 0.4$) samples calcined at 950°C

$$D = 0.89\lambda/\beta \cos \theta \quad (1)$$

where D is the crystallite size, λ is the wavelength of x-ray, β is the full width at half maximum (β expressed in radians), and θ is the Bragg's angle. The crystallite size obtained from XRD for different compositions is presented in Fig. 8. The oxides present an average crystallite size in the range of 25.5 – 46 nm indicating that the perovskite powders prepared by sol–gel method are composed of nanometric particles. It is observed that the crystallite size increases with increasing nickel content. This is probably due to the incorporation of Ni into the SrCoO_3 lattice which leads to the crystallite growth. A similar results were also found for $\text{LaCr}_{1-x}\text{Cu}_x\text{O}_3$ [41], $\text{LaAl}_{1-x}\text{Ni}_x\text{O}_{3-\delta}$ [42] and Mn-doped BaTiO_3 [43]. It has been shown that the growth of Mn-doped BaTiO_3 crystallite is promoted due to the increase in oxygen vacancies.

The morphologies of the $\text{SrCo}_{1-y}\text{Ni}_y\text{O}_{3-\delta}$ samples examined by SEM are shown in Fig. 9. The micrographs indicate that particles of different shapes and sizes were formed with very well pronounced agglomeration. It can be seen that particles did not show a distinct shape and the particle size is appreciated between 0.6 and $1.5\text{ }\mu\text{m}$. The grain boundaries are compact and there is only very small amounts of pores. The formation of agglomerates is probably due to the nature of the solvent used in the preparation of the gels. The same result was also found for samarium-doped ceria powders [44] and $\text{La}_{1-x}\text{Ca}_x\text{AlO}_3$ oxides [45]. It has been shown that treating the precipitate with water and ethanol allows interactions between particles, which leads during drying to the formation of chemical bonds.

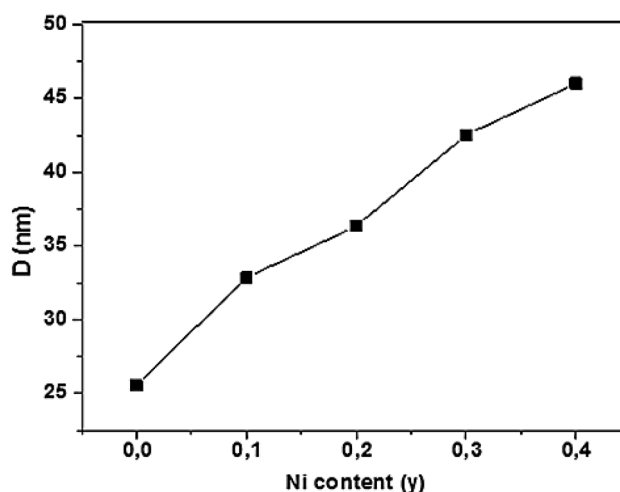


Fig. 8 Crystallite size of $\text{SrCo}_{1-y}\text{Ni}_y\text{O}_{3-\delta}$ ($0.0 \leq y \leq 0.4$) samples

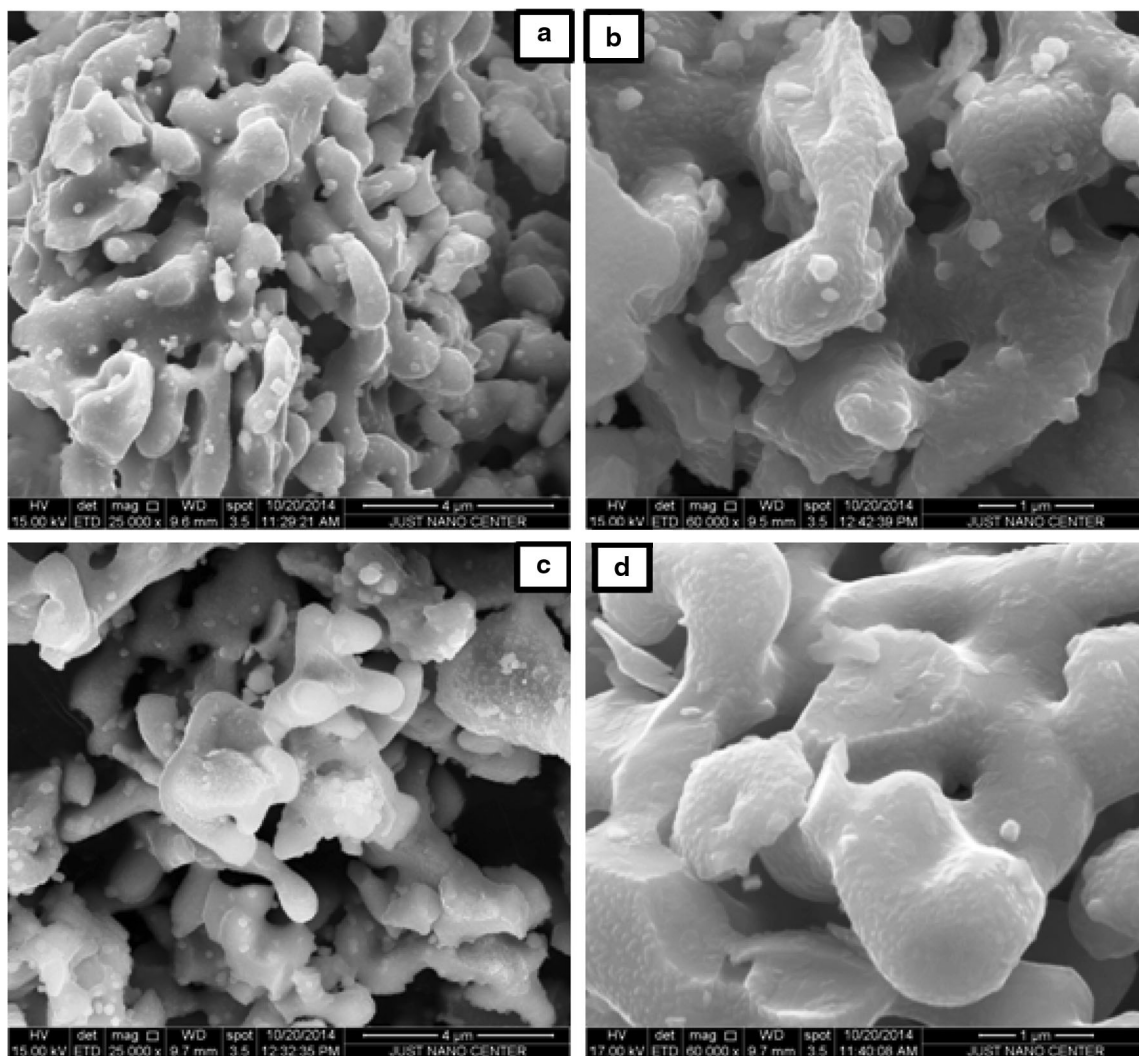


Fig. 9 SEM micrographs of $\text{SrCo}_{1-y}\text{Ni}_y\text{O}_{3-\delta}$. **a** $y = 0$; **b** $y = 0.1$; **c** $y = 0.2$ and **d** $y = 0.3$ calcined at 950°C

3.5 Electrical Conductivity Measurements

The temperature dependence of the electrical conductivity of the $\text{SrCo}_{1-y}\text{Ni}_y\text{O}_{3-\delta}$ ($y = 0, 0.1, 0.2, 0.3$ and 0.4) compounds in the temperature range $25^\circ\text{C} \leq T \leq 500^\circ\text{C}$ is presented in Fig. 10. All samples, exhibit the same tendency: the electrical conductivity increases with increasing temperature to a maximum value around 300°C indicating a semiconductor-type behavior and subsequently decreases with increasing temperature beyond 300°C , which indicates clearly that the temperature dependence of the conductivity is metallic. The substitution of Co by Ni ions induces an increase of the electrical conductivity compared to the non-substituted $\text{SrCoO}_{3-\delta}$ compound. The increase in the electrical conductivity is associated with the increase in Co^{4+} content and charge carriers in the system [46–48]. The Co^{4+} formation is induced by the substitution

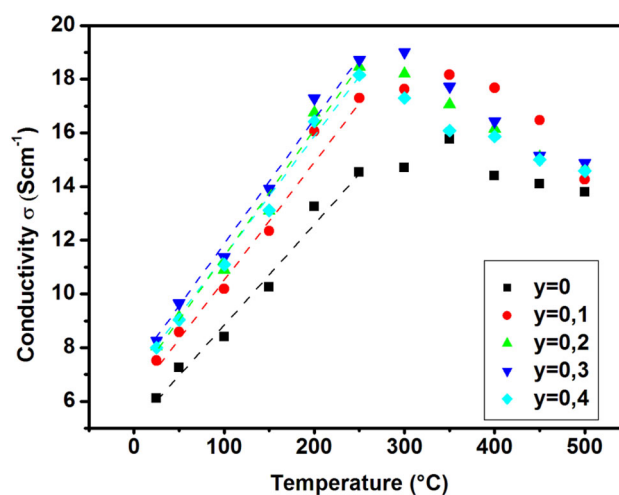


Fig. 10 Temperature dependence of the electrical conductivity of the SCNy samples ($y = 0, 0.1, 0.2, 0.3, 0.4$)

of the Co^{3+} by Ni^{2+} ions [47–49]. The same trends were found for $\text{LaCo}_{1-x}\text{Ni}_x\text{O}_3$ [47], $\text{Ln}(\text{Co,Ni})\text{O}_3$ [48] and $\text{La}_{0.9}\text{Sr}_{0.1}\text{Ga}_{1-x}\text{Ni}_x\text{O}_3$ [24].

The maximum electrical conductivity of 19 S cm^{-1} at around $300 \text{ }^\circ\text{C}$ was obtained for $\text{SrCo}_{0.7}\text{Ni}_{0.3}\text{O}_{3-\delta}$. This result indicates that electrical conductivity values in the whole range of temperatures are higher than those reported for $\text{La}_{0.9}\text{Sr}_{0.1}\text{Ga}_{1-x}\text{Ni}_x\text{O}_3$ [24]. The observed decrease in conductivity for the sample with $y = 0.4$ may be attributed to the solubility limit of Ni in the $\text{SrCoO}_{3-\delta}$. Nevertheless, it should be pointed out that the electrical conductivity of the polycrystalline $\text{SrCo}_{1-y}\text{Ni}_y\text{O}_{3-\delta}$ phases shows similar values compared to the electrical conductivity reported for hexagonal $\text{SrCoO}_{3-\delta}$ crystal [4].

Figure 11 shows the Arrhenius plot of $[\ln(\sigma \cdot T) \text{ vs } 1000 \text{ T}^{-1}]$ for $\text{SrCo}_{1-y}\text{Ni}_y\text{O}_{3-\delta}$ samples sintered at $950 \text{ }^\circ\text{C}$.

The activation energy of conduction was determined from the plot using the following expression derived for the small polaron mechanism [50]:

$$\sigma = \frac{A}{T} \exp\left(-\frac{E_a}{KT}\right) \quad (2)$$

where E_a is the activation energy of the conduction process, K is the Boltzmann constant and T is the absolute temperature and A the pre-exponential factor.

It can be seen from the curves that all the samples exhibit nonlinear variations in the whole temperature, suggesting two different conductive mechanisms. In fact, each curve presents two different slopes in the low and high temperature regions; the calculated activation energies in these regions are summarized in Table 2. This observation suggests that the electronic conduction is more predominant at the lower temperature region. Above $300 \text{ }^\circ\text{C}$, the ionic compensation is dominantly due the loss

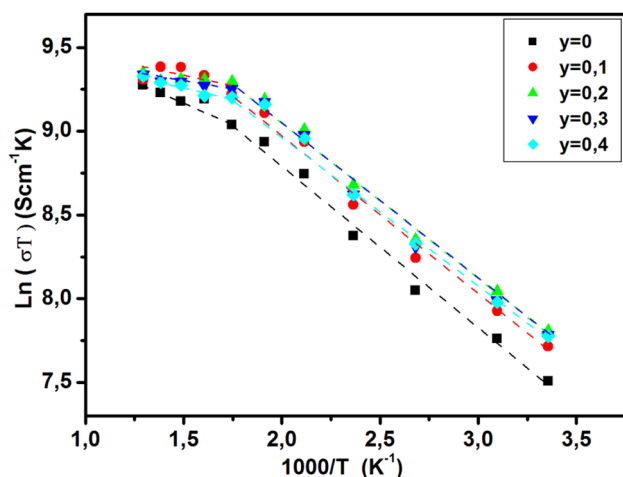


Fig. 11 Arrhenius plots of the SCNy ($y = 0, 0.1, 0.2, 0.3$ and 0.4)

of the lattice oxygen leading to a decrease of oxygen content of these oxides [51].

The activation energies at lower temperature range from 0.045 to 0.049 eV is closer to those reported in [5, 52]. It can be also noticed that the activation energy decreases with increasing Ni content. This trend indicates that the bandwidth increases with increasing Ni content [24].

3.6 Electrochemical Properties

The electrochemical activity for oxygen reduction and evolution reactions was investigated on $\text{SrCo}_{1-y}\text{Ni}_y\text{O}_{3-\delta}$ coated nickel substrate. The critical properties to consider when choosing an electrocatalyst support include its electrical conductivity surface area macromorphology microstructure corrosion resistance and cost [53]. The substrate of nickel satisfies these criteria and is often used in literature [54, 55].

Figures 12 and 13 shows the cathodic and anodic current-potential curves of air electrode with different substitutions of Nickel. The coated electrode films showed good adherence during polarization. The voltammograms exhibit two redox peaks, an anodic ($E_{pa} = 465 \text{ mV}$) and a corresponding cathodic ($E_{pc} = 290 \text{ mV}$) peak, prior to the onset of the O_2 evolution reaction, revealing a pseudo-capacitance due to the Ni(III)/Ni(II) surface redox couple [56, 57]. At lower current densities ($<20 \text{ mA cm}^{-2}$), the onset potential towards the oxygen evolution reaction is around 0.6 V vs Hg/HgO which is slightly higher than those reported in [58, 59]. All voltammograms show a wide plateau region which indicates that the coated perovskite electrodes present a wide range of electrochemical stability.

Electrode reactions over the surface of the oxides exhibit high currents. It is clear that at high doping level, the sample has a better electrochemical behavior in oxygen reduction and evolution reactions. Compared to all samples, the $\text{SrCo}_{0.7}\text{Ni}_{0.3}\text{O}_{3-\delta}$ one appears to be more active. Figure 14 presents the anodic and cathodic current densities obtained at potentials of $E = +1$ and -1.3 V , respectively.

The highest electrode performance is achieved, for both cases, with $y = 0.3$. Oxygen evolution reaction shows an important jump for $y > 0$, where the current density of $\text{SrCo}_{0.7}\text{Ni}_{0.3}\text{O}_{3-\delta}$ is three times greater than of $\text{SrCoO}_{3-\delta}$. The electrocatalytic activity of the perovskite oxides was greatly affected by the nature properties of B-site transition metal ions and the concentration of oxygen vacancies [60, 61].

In fact, Yu et al. [62] reported that the electrocatalytic activity toward methanol oxidation was affected by both the absorption of methanol as well as the electrical and oxygen ion conductivities. Furthermore, the higher

Table 2 Activation energy

Compounds	Activation energy (eV)	
	Lower temperature (25–300 °C)	Higher temperature (300–500 °C)
SrCoO _{3-δ}	0.0495	0.0397
SrCo _{0,9} Ni _{0,1} O _{3-δ}	0.0489	0.0197
SrCo _{0,8} Ni _{0,2} O _{3-δ}	0.0476	0.0100
SrCo _{0,7} Ni _{0,3} O _{3-δ}	0.0472	0.0150
SrCo _{0,6} Ni _{0,4} O _{3-δ}	0.0458	0.0254

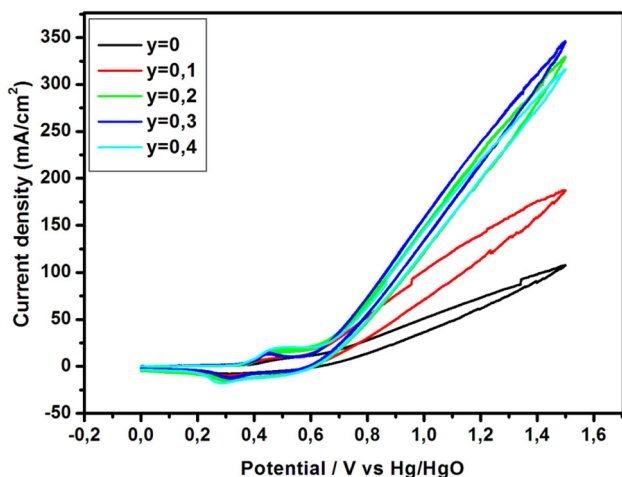


Fig. 12 Anodic polarization curves for SrCo_{1-y}Ni_yO_{3-δ} electrodes in 1 M KOH

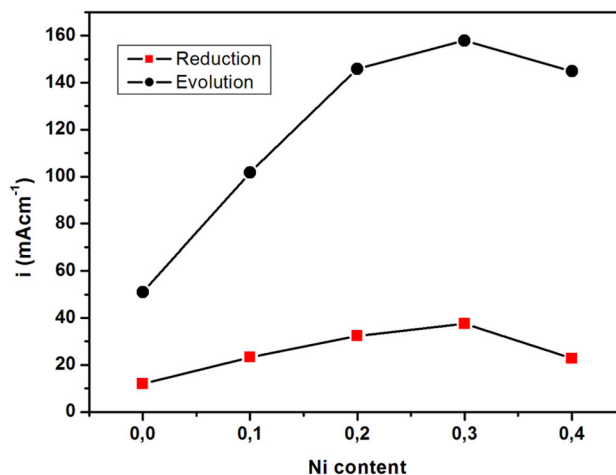


Fig. 14 Electrode performance as a function of Ni content at E = -1.3 and +1 V

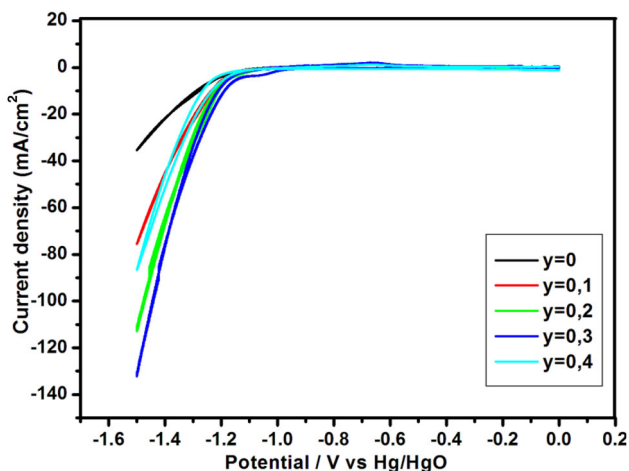


Fig. 13 Cathodic polarization curves for SrCo_{1-y}Ni_yO_{3-δ} electrodes in 1 M KOH

electrocatalytic activity for La_{1-x}Sr_xCuO_{3-δ} may be attributed to the capability of Cu ions for the absorption of methanol and the existence of a large amount of oxygen vacancies facilitating oxygen ion (O²⁻) transport.

Consequently, these results suggest that oxygen ion transport has an important contribution to the overall

electrical conduction in SrCo_{1-y}Ni_yO_{3-δ}. Indeed, previously works reported that oxygen stoichiometry is expected to be determinant in the electrical behavior [9, 12].

This correlation between the electrochemical activity and the electrical and oxygen ion conductivities play a key role in the optimization of these electrocatalysts.

4 Conclusion

The SrCo_{1-y}Ni_yO_{3-δ}, (0 ≤ y ≤ 0.4) perovskite oxides were prepared via sol-gel method. TG/DTA curves show the thermochemical behavior of the compound with respect to temperatures. XRD analysis reveals that all samples crystallize with rhombohedral structure at 950 °C, as well confirmed by IR spectroscopy. Single-phase perovskite structure was observed for SrCo_{1-y}Ni_yO_{3-δ} up to y = 0.30. The microstructure and morphology of the compounds show that the powders are constituted by the aggregation of various dimensions and forms of particles.

The electrical conductivity increases with increasing temperature to a maximum value around 300 °C indicating a semiconductor-type behavior. The substitution of Co by Ni ions induces an increase of the electrical conductivity

compared to the non-substituted $\text{SrCoO}_{3-\delta}$ compound. The maximum electrical conductivity of 19 S cm^{-1} at around $300 \text{ }^\circ\text{C}$ was obtained for $\text{SrCo}_{0.7}\text{Ni}_{0.3}\text{O}_{3-\delta}$.

In electrochemical study, $\text{SrCo}_{0.7}\text{Ni}_{0.3}\text{O}_{3-\delta}$ electrode exhibits significantly the greater electroactivity indicating that this material is the best electrocatalyst for oxygen reduction and evolution reactions in the investigated potential range. These results indicate clearly the correlation between the electrical conductivity and the electrochemical activity in these compounds.

Acknowledgments We wish to thank Professor B.A. Albiss, Jordan University of Science and Technology for carrying out electrical measurements.

References

- J.L. Tejuca, J.L.G. Fierro, *Properties and Applications of Perovskite-Type-Oxides* (Marcel Dekker, New York, 1993)
- M.T. Colomer, B.C.H. Steele, J.A. Kilner, *Solid State Ionics* **147**, 41 (2002)
- T. Hibino, A. Hashimoto, M. Suzuki, M. Sano, *J. Electrochem. Soc.* **149A**, 1503 (2002)
- A. Aguadero, D. Pérez-Coll, C. de la Calle, J.A. Alonso, M.J. Escudero, L. Daza, *J. Power Sources* **192**, 132 (2009)
- N.E. Trofimenko, J. Paulsen, H. Ullmann, R. Müller, *Solid State Ion.* **100**, 183 (1997)
- H.Y. Tu, Y. Takeda, N. Imanishi, O. Yamamoto, *Solid State Ion.* **100**, 283 (1997)
- Z.Q. Deng, W.S. Yang, W. Liu, C.S. Chen, *J. Solid State Chem.* **179**, 362 (2006)
- V.V. Vashook, M.V. Zinkevich, H. Ullmann, J. Paulsen, N. Trofimenko, K. Teske, *Solid State Ion.* **99**, 23 (1997)
- A. Maignan, C. Martin, N. Nguyen, B. Raveau, *Solid State Sci.* **3**, 57 (2001)
- F. Wang, Q. Zhou, T. He, G. Li, H. Ding, *J. Power Sources* **195**, 3772 (2010)
- P. Zeng, R. Ran, Z. Chen, W. Zhou, H. Gu, Z. Shao, S. Liu, *J. Alloys Compd.* **455**, 465 (2008)
- M.D. Carvalho, L.P. Ferreira, M.T. Colomer, P. Gacyszynski, M.M. Cruz, J.C. Waerenborgh, M. Godinho, *Solid State Sci.* **8**, 444 (2006)
- I.G.O. Crnivec, P. Djinic, B. Erjavec, A. Pintar, *Chem. Eng. J.* **207–208**, 299 (2012)
- M.M. Barroso-Quiroga, A.E. Castro-Luna, *Int. J. Hydrog. Energy* **35**, 6052 (2010)
- H. Ozdemir, M.A. Faruk Oksuzomer, M.A. Gurkaynak, *Int. J. Hydrog. Energy* **35**, 12147 (2010)
- G. Brunaccini, M. Lo Faro, D. La Rosa, V. Antonucci, A.S. Arico, *Int. J. Hydrog. Energy* **33**, 3150 (2008)
- M. Lebid, M. Omari, *Arab. J. Sci. Eng.* **39**, 147 (2014)
- Z. Hua Tan, X. Guo, *Ceram. Int.* **41**, 4953 (2015)
- J.C. Grenier, S. Ghodbane, G. Demaseau, M. Pouchard, P. Hagenmuller, *Mater. Res. Bull.* **14**(6), 831 (1979)
- Y. Takeda, R. Kanno, T. Takada, O. Yamamoto, M. Takano, Y. Bando, *Z. Anorg. Allg. Chem.* **540–541**, 259 (1986)
- J. Rodriguez, J.M. Gonzalez-Calbet, *Mater. Res. Bull.* **21**(4), 429 (1986)
- J. Rodriguez, J.M. Gonzalez-Calbet, J.C. Grenier, J. Pannetier, M. Anne, *Solid State Commun.* **62**(4), 231 (1987)
- R.D. Shannon, *Acta Crystallogr. A* **32**, 751 (1976)
- M.T. Colomer, J.A. Kilner, *Solid State Ion.* **182**, 76 (2011)
- Y. Liu, G. Zhu, B. Ge, H. Zhou, A. Yuan, X. Shen, *Cryst. Eng. Comm.* **14**, 6264 (2012)
- X.H. Xia, J.P. Tu, Y.Q. Zhang, Y.J. Mai, X.L. Wang, C.D. Gu, *RSC Adv.* **2**, 1835 (2012)
- Z. Wen, L. Zhu, Y. Li, Z. Zhang, Z. Ye, *Sens. Actuators B* **203**, 873 (2014)
- M. Tatzber, M. Stemmer, H. Spiegel, C. Katzberger, G. Haberhauer, M.H. Gerzabek, *Environ. Chem. Lett.* **5**, 9 (2007)
- B. Šoptrajanov, V. Stefov, I. Kuzmanovski, G. Jovanovski, H.D. Lutz, B. Engelen, *J. Mol. Struct.* **613**, 7 (2002)
- M.Y. Nassar, I.S. Ahmed, *Polyhedron* **30**, 2431 (2011)
- B. Sreedhar, M. Sulochana, Ch. Satya Vani, D. Keerthi Devi, N.V. Subba Naidu, *Eur. Chem. Bull.* **3**(3), 234 (2014)
- P. Ptáček, E. Bartoničková, J. Švec, T. Opravil, F. Šoukal, F. Frajkorová, *Ceram. Int.* **41**, 115 (2015)
- M. Sun, Y. Jiang, F. Li, M. Xia, B. Xue, D. Liu, *Mater. Res. Bull.* **46**, 801 (2011)
- A. Leleckaite, A. Kareiva, *Opt. Mater.* **26**, 123 (2004)
- B. Schrader, *Infrared and Raman Spectroscopy. Methods and Applications* (VCH, Weinheim, 1995)
- K. Agilandeswari, A. Ruban Kumar, *Superlattice Microstruct.* **68**, 27 (2014)
- D.S. Melo, E.P. Marinho, L.E.B. Soledade, D.M.A. Melo, S.J.G. Lima, E. Longo, I.M.G. Santos, A.G. Souza, *J. Mater. Sci.* **43**, 551 (2008)
- A. Baranauskas, D. Jasaitis, A. Kareiva, *Vibr. Spectrosc.* **28**, 263 (2002)
- H. Cui, M. Zayat, D. Levy, *J. Non-Cryst. Solids* **352**, 3035 (2006)
- B.D. Cullity, *Elements of X-ray Diffractions* (Addison Wesley, Reading, 1978)
- K. Adaika, M. Omari, *J. Sol–Gel. Sci. Technol.* **75**, 298 (2015)
- L. Djoudi, M. Omari, *J. Inorg. Organomet. Polym.* **25**, 796 (2015)
- H.I. Hsiang, F.S. Yen, Y.H. Chang, *J. Mater. Sci.* **31**, 2417 (1996)
- G.B. Jung, T.J. Huang, M.H. Huang, C.L. Chang, *J. Mater. Sci.* **36**, 5839 (2001)
- M. Diafi, M. Omari, *Bol. Soc. Esp. Ceram. Vidr.* **51**(6), 337 (2012)
- R. Robert, L. Bocher, M. Trottmann, A. Reller, A. Weidenkaff, *J. Solid State Chem.* **179**, 3867 (2006)
- F. Li, J.F. Li, *Ceram. Int.* **37**, 105 (2011)
- R. Robert, M.H. Aguirre, P. Hug, A. Reller, A. Weidenkaff, *Acta Mater.* **55**, 4965 (2007)
- Y. Kobayashi, S. Murata, K. Asai, J.M. Tranquada, G. Shirane, K. Kohn, *J. Phys. Soc. Jpn.* **68**(3), 1011 (1999)
- S. Liping, H. Lihua, Z. Hui, L. Qiang, C. Pijolat, *J. Power Sources* **179**, 96 (2008)
- S. Lu, B. Yu, X. Meng, X. Zhao, Y. Ji, C. Fu, Y. Zhang, L. Yang, H. Fan, *J. Power Sources* **273**, 24 (2015)
- B. Qu, W. Long, F. Jin, S. Wang, T. He, *Int. J. Hydrog. Energy* **39**, 12074 (2014)
- W. Li, X. Wang, Z. Chen, M. Waje, Y. Yan, *J. Phys. Chem. B* **110**(15353), 55 (2006)
- R.N. Singh, A. Singh, D. Mishra, Anindita, P. Chartier, *J. Power Sources* **185**, 776 (2008)
- B. Lal, M.K. Raghunandan, M. Gupta, R.N. Singh, *Int. J. Hydrog. Energy* **30**, 723 (2005)
- R.N. Singh, J.-F. Koenig, G. Poillerat, P. Chartier, *J. Electrochem. Soc.* **137**, 1408 (1990)
- M.A. AbdelRahim, R.M. AbdelHameed, M.W. Khalil, *J. Power Sources* **134**, 160 (2004)
- T. Kudo, H. Obayashi, T. Geji, *J. Electrochem. Soc.* **122**, 159 (1975)
- M. Shimada, M. Koizumi, *J. Appl. Electrochem.* **12**, 275 (1982)
- J.H. White, A.F. Sammells, *J. Electrochem. Soc.* **140**, 2167 (1993)
- V. Raghuvveer, K.R. Thampi, N. Xanthopoulos, H.J. Mathieu, B. Viswanathan, *Solid State Ion.* **140**, 263 (2001)
- H.C. Yu, K.Z. Fung, T.C. Guo, W. Li Chang, *Electrochim. Acta* **50**, 811 (2004)